Surface Science 602 (2008) L74–L78

Contents lists available at ScienceDirect

Surface Science

journal homepage: www.elsevier.com/locate/susc

Surface Science Letters

Formation mechanisms of polar and non-polar amorphous oxide–semiconductor interfaces

Evgueni A. Chagarov *, Andrew C. Kummel

Department of Chemistry and Biochemistry, University of California, San Diego, La Jolla, CA 92093, United States

ARTICLE INFO

Article history:
Received 26 February 2008
Accepted for publication 11 April 2008
Available online 4 May 2008

Keywords:
Density functional theory
Molecular dynamics
High-κ oxide
Amorphous oxide
Oxide–semiconductor interface

ABSTRACT

The formation mechanisms of polar and nonpolar interfaces were investigated by density-functional theory molecular dynamics simulations of the atomic structure of the a-Al_2O_3/Ge(100)(2 × 1) and a-ZrO_2/Ge(100)(2 × 1) interfaces. The a-Al_2O_3/Ge interface demonstrates strong chemical selectivity resulting in interface bonding exclusively through Al–O–Ge bonds. The a-ZrO_2/Ge interface has both Zr–O–Ge and O–Zr–Ge bonds. The a-ZrO_2/Ge junction creates a much less polar interface with lower deformation and intermixing than a-Al_2O_3/Ge consistent with experimental measurements. In both cases, the interface polarity is determined by the stoichiometry of the interface bonding as opposed to charged defect formation.

The rapid scaling of complementary metal oxide semiconductor (CMOS) technology requires substituting the traditional gate oxide, SiO_2, with amorphous high-κ dielectrics, which can maintain the same capacitance with much lower leakage current. The leading candidates for such high-κ gate amorphous oxide materials include a-Al_2O_3 and a-ZrO_2. Ge is one of a few semiconductors that can offer significantly higher hole mobility than silicon and, therefore, is being extensively investigated for p-channel high-κ MOSFETs.

Although there are previously reported density-functional theory (DFT) simulations of high-κ oxide–semiconductor interfaces, to our knowledge there is only one report on amorphous oxide bonding, and this oxide contains a SiO_2 interlayer so it lacks direct amorphous high-κ oxide–semiconductor bonds [1–3]. Amorphous oxide–semiconductor interfaces are likely to be superior to crystalline oxide–semiconductor interfaces because the large differences in unit cell sizes prevent growth of crystalline oxides on semiconductors without a high density of defects. Whereas many previously reported simulations of oxide–semiconductor interfaces were limited to artificially formed structures relaxed at 0 K, this study employs DFT molecular dynamics (DFT-MD) at finite temperatures thereby providing the system with enough freedom to naturally evolve into the most realistic state.

Amorphous a-Al_2O_3 and a-ZrO_2 samples were generated using a hybrid "melt and quench" approach whereby classical MD simulations were performed prior to DFT annealing. Classical MD simulations were performed by a LAMMPS simulator, expanded by empirical potentials for Al_2O_3 [4] and ZrO_2 [5]. All DFT simulations were performed with the VASP package using PAW pseudopotentials and the PBE exchange-correlation functional [6–9].

The stoichiometric a-Al_2O_3 and a-ZrO_2 samples contain 100 and 96 atoms, respectively. The classical MD generation sequence was started by high-temperature annealing at 5000 K from a low-density ordered oxide phase, which provided very good oxide intermixing. After annealing at low density (ρ_{norm}/ρ_{low} = 3.38), the periodic boundary condition (PBC) box and the whole sample were homogeneously and instantaneously rescaled back to the normal amorphous oxide density and annealed at 5000 K. The system was then linearly cooled to room temperature (RT) and thermally equilibrated (EPAPS Fig. 1).

To test that sufficient intermixing occurs during the classical annealing procedure, the average atom displacements were calculated. During Al_2O_3 high-T (5000 K) annealing at low density, the final average atom displacement was 7.6 Å or ~70% of the smallest PBC lattice vector (11.0 Å). During the high-T Al_2O_3 annealing at normal density, the average atom displacement was 5.1 Å or ~65% of the smallest lattice vector (7.8 Å). The similar atomic displacement values for a-ZrO_2 were 7.9 Å (53%) and 5.46 Å (54%), respectively. Note that these values are a slight underestimation of the real atom displacement since some atoms cross the PBC box and reappear on its other side. The total velocity integration over time indicates an absence of oxide correlated macroscopic motion through PBC boundaries. The high values of average atomic displacement during high-T annealing phases were consistent with

* Corresponding author. Tel.: +1 813 263 0192.
E-mail address: echagaro@ucsd.edu (E.A. Chagarov).

0039-6028/$ - see front matter © 2008 Elsevier B.V. All rights reserved.
doi:10.1016/j.susc.2008.04.026

the high degree of the melt intermixing important for amorphous sample generation.

The properties of classical a-Al_2O_3 and a-ZrO_2 samples are sensitive to the cooling rate and annealing time at low density. These two parameters were varied such that 24 different preparation sequences with 24 different final amorphous samples for each sample type were investigated. Each classical amorphous sample was thoroughly analyzed by nearest neighbor distribution and radial-distribution functions (RDF) averaged over 2001 structure snapshots spaced by 10 fs intervals at RT. The RDFs were employed to calculate the main peak positions and their FWHM, the average nearest neighbor numbers, and the neutron scattering static structure functions. Since experimental data on the a-Al_2O_3 and a-ZrO_2 microstructures are limited, both experimental and selected simulation data were used for reference sample properties [10–15]. The available simulated reference for a-Al_2O_3 was classically generated [11], whereas the reference for a-ZrO_2 was DFT generated [12–14]; therefore, a small variation in the sample selection procedure was introduced.

The most realistic classical a-Al_2O_3 sample was prepared at a density of 3.20 g/cm^3 with the annealing/cooling timing presented in Table 1. Experimental data report amorphous Al_2O_3 states over a 3.05–3.40 g/cm^3 density range [16,17], while computer simulations demonstrated successful generation at 3.0–3.3 g/cm^3 [11,18,19]. The classical density of our a-Al_2O_3 sample is supported by previous classical simulations of a-Al_2O_3 demonstrating good correlation with experiment [10,11]. The selected classical a-Al_2O_3 sample agrees well with experimental and classical MD nearest neighbor distributions (Table 2), average nearest neighbor numbers, RDF peaks, and neutron static structure functions [10,11]. The RDF main peak positions for Al–O, O–O, Al–Al bonds in our sample are 1.77 Å, 2.82 Å, 3.07 Å, respectively, versus 1.76 Å, 2.75 Å, 3.12 Å (classical MD) [11], and experimental 1.8 Å, 2.8 Å, 3.2 Å [10]. The slight deviation in our sample properties from previously reported samples [10,11] is consistent with our sample having only 100 atoms in comparison with 1800 atoms in Ref. [11] and a macroscopic experimental sample in Ref. [10].

The most realistic classical a-Al_2O_3 sample was rescaled to a DFT density of 3.26 g/cm^3. The ratio of classical to DFT density was determined with a separate classical sample, which was DFT annealed by the same procedure and finally relaxed at variable volume. The resulting DFT sample size was $\sim$11.58 $\times$ 11.58 $\times$ 7.8 Å. This rescaled sample was then DFT annealed for 1000 fs at 1500 K, linearly cooled to 0 K for 200 fs and relaxed to the ground state with a 0.01 eV/Å force tolerance level (EPAPS Fig. 1). The stress tensor components of the DFT annealed amorphous sample were analyzed to verify the absence of internal hydrostatic pressure. All presented DFT runs were performed with 1 fs timesteps. The Density of States (DOS) for the DFT a-Al_2O_3 sample resulted in a defect state free bandgap of 3.80 eV, in excellent agreement with a previously reported DFT band gap of 3.77 eV [18].

The 24 different classical a-ZrO_2 samples were prepared using the same general procedure as a-Al_2O_3 at 4.71 g/cm^3 density, but with a different annealing/cooling timing. The classical amorphous density was determined from the a-ZrO_2 DFT amorphous density and the classical-to-DFT density correction ratio. The properties of the 24 samples were compared to previous DFT simulations [12–14] and experimental data [15]. The classical generation timing of the selected sample is presented in Table 1. Published DFT simulations generated realistic amorphous a-ZrO_2 systems within a 4.86–5.32 g/cm^3 density range [12,13]. The density of 4.90 g/cm^3 was selected to be far from higher crystalline ones to minimize the risk of sample recrystallization. The sizes of our DFT samples are $\sim$11.58 $\times$ 11.58 $\times$ 10.0 Å. The three classical a-ZrO_2 samples demonstrating the smallest deviation in nearest neighbor distribution from the properties of the DFT sample in Ref. [13] were rescaled to a DFT density of 4.90 g/cm^3, DFT annealed at 2800 K for 1000 fs, cooled to 0 K for 200 fs and relaxed. The nearest neighbor distribution deviation from the sample of Ref. [13] was estimated, and the sample with the closest match was selected (Table 3). The stress tensor components of the selected DFT annealed amorphous sample were analyzed to verify the absence of internal hydrostatic pressure.

The nearest neighbor distribution of our DFT a-ZrO_2 sample demonstrates a good match to the distribution of the DFT sample from Ref. [13] (Table 3). The calculated RDF functions for the DFT annealed a-ZrO_2 sample indicate Zr–O main peak at 2.1 Å and Zr–O bond lengths distribution primarily in the interval between 2.0–2.3 Å, correlating well with previously reported bond lengths of 2.04–2.25 Å [12]. The RDF curves for Zr–Zr and O–O indicate the main peak at 3.5 Å and 2.8 Å, respectively. The DOS calculations resulted in a defect state free bandgap of $\sim$2.7 eV, versus previously reported values of $\sim$3.2 eV (DFT, ρ = 5.32 g/cm^3) [14], and 4.7 eV (experimental) [15]. This discrepancy with experiment is consistent with the standard band-gap underestimation typical for GGA DFT without exact exchange interaction.

The initial Ge(100)(2 $\times$ 1) surface reconstruction was created by the DFT relaxation of a 64 atom Ge slab with a DFT lattice constant, forming area of $\sim$11.58 Å $\times$ 11.58 Å with $\sim$10.4 Å slab thickness. During relaxation, the three bottom layers were fixed in their bulk positions. The Ge atoms at the bottom surface were terminated with H atoms. The amorphous sample sizes at the classical MD stage were chosen so that after rescaling from classical to DFT density they would perfectly match the Ge(100) surface area.

The periodic boundary conditions of the DFT relaxed bulk a-Al_2O_3 and a-ZrO_2 samples were broken in the vertical direction by adding $\sim$12 Å of vacuum space. The plane of sectioning was chosen to provide approximately equal numbers of metal and oxygen at the surface. The oxide sample was placed on the relaxed Ge(2 $\times$ 1) reconstructed surface at a height that ensured the Al–

Table 1
Timing for different stages of classical MD generation of the selected a-Al_2O_3 and a-ZrO_2 samples

	Stage 1 (ps)	Stage 2 (ps)	Stage 3 (ps)	Stage 4 (ps)
a-Al_2O_3	350	400	100	100
a-ZrO_2	500	500	100	100

Stage1-annealing at 5000 K at low density, Stage 2-annealing at 5000 K at normal amorphous density, Stage 3-cooling to RT and Stage 4-equilibration at RT.

Table 2
Nearest neighbor distribution of our classical a-Al_2O_3 sample vs. classical sample of Ref. [11]. Cutoff radius −2.2 Å

Nearest neighbor distribution	O(2)	O(3)	O(4)	Al(3)	Al(4)	Al(5)	Al(6)
Our sample (%)	22	75	3	0.0	78	22	0.0
Ref. [11] (%)	20	78	2	0.3	76	22	1.7

Table 3
Nearest neighbor distribution of our DFT annealed a-ZrO_2 sample vs. DFT generated sample [12,13]

Nearest neighbor distribution	O(2)	O(3)	O(4)	O(5)	Zr(5)	Zr(6)	Zr(7)	Zr(8)
Our sample	4	40	19	1	6	11	13	2
Refs. [12,13]	2	43	18	1	2	12	16	2

Nearest neighbor distribution is in absolute units. Both samples have equal number of atoms. Cutoff radius is 3 Å.

Ge or Zr–Ge pair lengths were approximately equal to 1/2–3/4 of their empirical bond lengths. The initial oxide surface was not relaxed after bulk cutting, thereby generating a chemically active oxide surface with dangling bonds in contact with reconstructed Ge. The upper surface of the oxide was saturated by H atoms filling every dangling bond with ~12 Å of vacuum above to avoid spurious interaction through the PBC. The oxide/semiconductor interface was simulated with one interface and vacuum (Fig. 1) instead of building a supercell model with two oxide/semiconductor interfaces and no vacuum. This single interface model minimizes unphysical constraints for atomic chemical migration to/from the oxide/semiconductor interface for the thin oxide (~10 Å) layers. To compensate spurious electric field induced by PBC for this type of system, a dipole correction was applied [20–22]. Prior to generating the amorphous oxide/Ge stack, the relaxed amorphous sample was verified to be free of internal hydrostatic pressure. Formation of the oxide/Ge with a vacuum spacer minimizes the creation of additional hydrostatic pressure, and annealing of the oxide/semiconductor stack with vacuum layer over oxide provides an additional channel for internal stress relief. We have tried both supercell and one-interface designs and found that for amorphous/crystalline interface with its irregular and complex bonding structure, the supercell design easily got locked vertical stresses in the system leading to distortion of electronic structure and interface bonding.

To model the oxide/semiconductor bonding, all Ge atoms were fixed and an initial partial relaxation of the oxide was performed using the conjugate-gradient (CG) algorithm for 20–30 CG steps. The length of this stage was determined by performing a longer run (~150 CG steps), and it was found that 20–30 steps were sufficient for the oxide/Ge interface to reach a realistic bonding distance and for the oxide to adjust to the Ge row/trough topology. After the initial 20–30 CG steps with all Ge atoms frozen, all atoms were unfrozen except for the bottom 3 Ge layers, and the whole system was annealed at 700 K for 1000 fs. After annealing, the system was cooled to 0 K for 200 fs and relaxed to the ground state with a 0.05 eV/Å force tolerance level. Since the PBC box was relatively big and the DFT runs included ~200 atoms and ~2500 time steps, the initial relaxation, annealing, cooling and final relaxation were performed with 2 irreducible k-points for computational efficiency. After the final relaxation, the k-point set was expanded to a $3 \times 3 \times 1$ mesh, and the system was refined by an additional relaxation (~20–50 steps) at a force tolerance level 0.05 eV/Å so that the small forces introduced by the k-point expansion were removed. While this had no visible effect on the system geometry, it could improve the electronic structure.

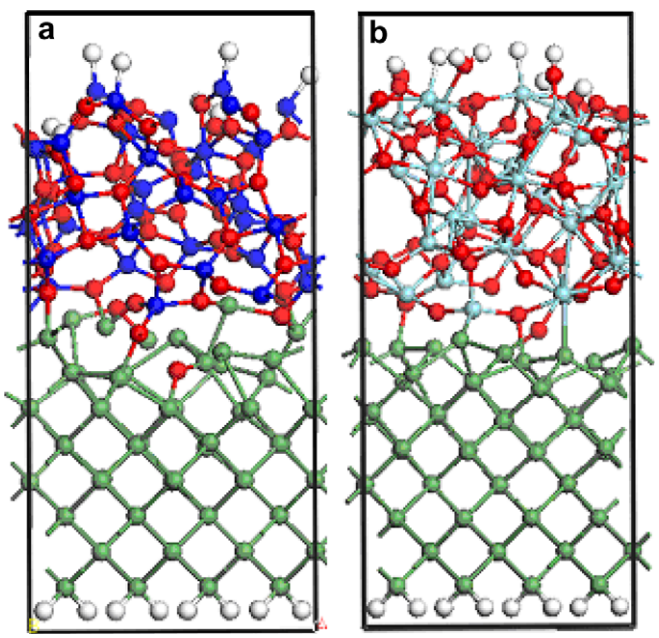

Fig. 1. (a) a-Al_2O_3/Ge(100)(2×1) and (b) a-ZrO_2/Ge(100)(2×1) interfaces after final relaxation. Ge-green, O-red, Al-dark blue, Zr-light blue. (For interpretation of the references to colour in this figure legend, the reader is referred to the web version of this article.)

During annealing, the a-Al_2O_3/Ge interface shows a very clear chemical segregation: Al atoms migrate out of interface into the oxide bulk, while O atoms migrate to the interface (Fig. 1a). This creates an O-rich interface with the oxide bonding to Ge predominantly through Al–O–Ge bonds with few or no O–Al–Ge ones. This phenomenon of oxide surface oxygen enrichment was previously observed by classical MD for clean a-Al_2O_3 surfaces [19], DFT simulations for (0001) interfaces of α-alumina and (001) interfaces of crystalline κ-alumina with vacuum [23,24], and was confirmed by our DFT simulations for clean a-Al_2O_3 and a-ZrO_2 vacuum interfaces.

The a-Al_2O_3/Ge interface demonstrates a moderate deformation of Ge dimer layers. Some Ge dimer atoms are pulled up by the oxide hence distorting the Ge surface and creating vacancies that facilitate O diffusion. Analysis of Ge atoms at the interface indicates that a partition of 4- and 3-coordinated Ge is ~45% for each type with the remainder being 2-coordinated. Most of the 3-fold coordinate Ge atoms are ones which do not have bonds to oxide. The 2-coordinated Ge atoms are those which are pulled out of the Ge slab and are only bonded to oxygen. The clean reconstructed Ge(100)(2×1) surface is formed exclusively by 3-fold coordinated atoms. The O atoms forming bonds to Ge have an approximately equal partition of 2- and 3-coordination. To investigate charge transfer at the interface, a Bader charge analysis was performed. The Ge atoms bonded to O lose ~0.7–1.0 |e|. To estimate the total charge transfer to/from Ge substrate, the difference in the total Bader charge on all Ge atoms and their passivating H atoms in the oxide/Ge model vs in the clean Ge model was calculated. This analysis demonstrated that after formation of the a-Al_2O_3/Ge interface (Fig. 1-a), the Ge substrate lost ~9.23 |e| of charge, resulting in -6.9×10^{-2} |e|/Å^2 of charge transfer. This large interfacial dipole would have an adverse effect on device performance.

DFT annealing of the a-ZrO_2/Ge interface reveals a different structural pattern (Fig. 1b). During annealing at 700 K the interface has approximately 1.5 times more long Zr–Ge bonds (empirical length ~3 Å) than short O–Ge bonds (empirical length ~2 Å) with a propensity for the oxygen atoms to bridge between pairs of Zr. However after cooling and final relaxation, more O–Ge bonds are established leading to roughly equal numbers of Zr–Ge and O–Ge bonds. This is consistent with the thermally excited interface being slightly wider than the low temperature interface thereby favoring longer Zr–Ge (~3.0 Å) bonds compared to the shorter O–Ge (~2.0 Å) bonds. During the final relaxation, the interface region is densified, decreasing the average interatomic distance and creating additional O–Ge bonds roughly balancing the number of Zr–Ge ones (Fig. 1b).

A coordination analysis indicates that interfacial O and Ge atoms have an approximately equal partition of 2-,3- and 3-,4-coordinated atoms, respectively, at the a-ZrO_2/Ge interface. Note that no 2-fold coordinate Ge was observed. The interfacial Zr atoms forming bonds to Ge have a wide nearest neighbor distribution ranging between 4 and 7. A Bader charge analysis of the charge transfer after interface formation indicates that Ge atoms bonded to O lose ~0.6–0.8 |e|, while Ge atoms bonded to Zr increase their atomic charge by ~0.5 |e|. The a-ZrO_2/Ge interface (Fig. 1b) depleted the whole Ge substrate by only ~0.40 |e|, which gave -3.0×10^{-3} |e|/Å^2 of the total charge transfer. The fact that a-

ZrO_2/Ge interface demonstrates ~23× lower charge transfer from Ge than a-Al_2O_3/Ge is consistent with the interface with O–Zr–Ge and Zr–O–Ge bonds having compensating bond dipoles while the a-Al_2O_3/Ge interface with only Al–O–Ge bonds has only unidirectional bond dipoles from Ge to a-Al_2O_3 bulk.

The interface roughness is an important factor for solid state device performance since it degrades carrier mobility. The comparative analysis of Fig. 1 reveals that the a-Al_2O_3/Ge interface creates a larger deformation of Ge and intermixing than a-ZrO_2/Ge. To quantify Ge substrate deformation, the average Ge positional deviation per horizontal layer with respect to the relaxed clean Ge(100)(2 × 1) slab was calculated using the following norm: $\Delta\bar{R}_i = \frac{1}{N_i}\sum_j |\bar{R}_j - \bar{R}_{0j}|$, where N_i is the number of Ge atoms in horizontal layer i, $\bar{R}_j$ and $\bar{R}_{0j}$ are coordinates of Ge atom j belonging to the horizontal layer i after the interface relaxation and in the initial relaxed clean Ge(100)(2 × 1) slab, while index j goes along every Ge atom in horizontal layer i. The average Ge deviation per layer is presented in EPAPS Fig. 2. The first three layers have zero deviation since they are fixed in their bulk positions. The Ge(100)(2 × 1) slab has 8 atoms per layer. For the a-Al_2O_3/Ge interface, the top two Ge surface dimer atoms (layers 8 and 9) deviate on average 1.3 and 2.5 Å, respectively, while the same dimer atoms in the a-ZrO_2/Ge interface deviate on average 1.0 and 0.9 Å, respectively. This is consistent with differences in the bulk moduli and the ADF of the two amorphous oxides. The ADF functions for DFT annealed a-Al_2O_3 and a-ZrO_2 samples indicate a broader distribution of O–Zr–O angles with a standard deviation of 28.7° compared to O-Al-O angles with a standard deviation of 23.7°. The broader range of O–Zr–O angles indicates the greater flexibility of a-ZrO_2 in comparison with a-Al_2O_3 and is consistent with smaller Ge deformation in the a-ZrO_2/Ge interface (Fig. 1). The DFT calculated bulk moduli of a-Al_2O_3 and a-ZrO_2 bulk samples are 96.9 and 77.9 GPa, respectively, demonstrating the higher compression resistance of a-Al_2O_3. The DFT bulk modulus of crystalline Ge bulk is 57.8 GPa.

Interfacial reactions might also be responsible for greater interfacial roughness of the a-Al_2O_3/Ge vs a-ZrO_2/Ge interface. The Gibbs energy change of possible interfacial chemical reactions is estimated for O transfer from the oxide to the substrate forming GeO_2 or GeO oxides. Creation of the GeO_2 oxide was found to be endothermic and required 537.1 kJ/mol and 520.6 kJ/mol (normalized to one GeO_2 formula unit) for a-Al_2O_3/Ge and a-ZrO_2/Ge interfaces, respectively. Creation of the GeO interfacial oxide is also endothermic requiring 296.7 kJ/mol and 288.4 kJ/mol (normalized to one GeO formula unit) for a-Al_2O_3/Ge and a-ZrO_2/Ge interfaces, respectively. The temperature-dependent term is not significant enough to cause reaction exothermicity at reasonable processing temperatures. Note that interfaces often are not stoichiometric, which can significantly affect Gibbs energy change for interfacial reactions in oxygen-rich conditions. Therefore the presented values can be considered only as estimates for interfacial oxide GeO_x ($1 \le x \le 2$) formation. The fact that O transfer reactions for a-Al_2O_3/Ge and a-ZrO_2/Ge interfaces are endothermic and close in absolute values indicates that intermixing at the a-Al_2O_3/Ge interface should be attributed mainly to kinetic rather than thermodynamic interface phenomena.

To further verify the greater interfacial roughness of a-Al_2O_3/Ge vs a-ZrO_2/Ge interfaces, the same DFT simulations were performed at an elevated (1100 K) annealing temperature that effectively increased the timescale. This fails to induce significant changes in bonding at the a-ZrO_2/Ge interface, while for a-Al_2O_3/Ge it led to a slightly larger interface deformation, intermixing, and void formation. The interface chemical segregation for a-Al_2O_3/Ge interface was found to be very fast, first ~100 fs.

The observed difference in roughness of a-Al_2O_3/Ge and a-ZrO_2/Ge interfaces demonstrates a very good correlation with experimental measurements. The available HR-TEM images of a ZrO_2/Ge stack reported no interfacial layer after annealing at 700 K [25–27], while EELS profiles showed very little Ge diffusion into ZrO_2 [28], which correlates well with no intermixing (Fig. 1b). Conversely, the experimental measurements of a Al_2O_3/Ge stack indicated an interfacial layer (IL) thickness of ~10 Å [29]. The presence of an interfacial layer with some intermixing in experimental data correlates well with our simulation results (Fig 1a). The thickness of our a-Al_2O_3/Ge intermixed layer, which is an initial phase of IL formation, is several times smaller than the experimental one, since the DFT annealing timescale is much less than the timescale of experimental annealing. Despite this limitation, our DFT simulations were able to predict general trends of interface formation and roughness. While no experimental data is available upon the dynamics of polar vs nonpolar interface formation, the consistency of the experimental results with the DFT molecular dynamics calculations for the structure of the amorphous oxide/Ge interfaces is consistent with the basic mechanisms proposed in this study: the a-Al_2O_3/Ge interface demonstrates strong chemical selectivity resulting in a polar interface bonding exclusively through Al–O–Ge bonds while the a-ZrO_2/Ge interface has both Zr–O–Ge and O–Zr–Ge bonds creating a nonpolar interface.

DFT MD is a very accurate simulation technique, which requires significant computational resources and time. Although better statistics can be obtained by performing many simulations with different samples and initial configurations, the very high cost of DFT MD runs make this impractical within reasonable time at modern computational facilities. The generation of another realistic classical sample and its subsequent DFT annealing would provide a sample with different atomic arrangement, but very similar averaged bulk properties such as RDF's, coordination distributions, and average coordination numbers because only these samples would pass realism test by comparison to the reference sample. The initial interface atomic arrangement has wider variation from system to system. However investigation of amorphous/crystalline interface makes the initial configuration more robust and general since amorphous surface with its high level of randomization inherently provides enhanced level of generality by sampling much more possibilities of initial interatomic bonding in configuration space of oxide/semiconductor interface. Performing DFT MD at finite temperature adds a whole new dimension of realism by probing different interface bonding configurations over time. The facts that our results demonstrate good correlation to experimental data and interface annealing at the elevated (1100 K) temperature leads to the same qualitative results as data presented here support generality and reliability of the presented a-Al_2O_3/Ge and a-ZrO_2/Ge interface evolution simulations.

Acknowledgements

We would like to thank Jim Adams (ASU), Matthias Passlack (Freescale), Paul McIntyre (Stanford U) and Wilman Tsai (Intel) for useful discussions. This research was funded by FCRP-MSD (887.011) and Intel/UCDISCOVERY.

Appendix A. Supplementary material

Supplementary data associated with this article can be found, in the online version, at doi:10.1016/j.susc.2008.04.026.

References

[1] K.-Y. Tse, J. Robertson, J. Appl. Phys. 100 (2006) 093713.
[2] J.-H. Ha, K.-I. Seo, P.C. McIntyre, K.C. Saraswat, K. Cho, Appl. Phys. Lett. 90 (2007) 112911.
[3] P. Broqvist, A. Pasquarello, Microelectr. Eng. 84 (2007) 2022.

[4] M. Matsui, Miner. Mag. 58A (1994) 571.
[5] P. Schelling, S. Phillpot, D. Wolf, J. Am. Ceram. Soc. 84 (7) (2001) 1609.
[6] P.E. Blöchl, Phys. Rev. B 50 (1994) 17953.
[7] G. Kresse, J. Joubert, Phys. Rev. B 59 (1999) 1758.
[8] J.P. Perdew, K. Burke, M. Ernzerhof, Phys. Rev. Lett. 77 (1996) 3865.
[9] J.P. Perdew, K. Burke, M. Ernzerhof, Phys. Rev. Lett. 78 (1997) 1396.
[10] P. Lamparter, R. Kniep, Physica B 234–236 (1997) 405.
[11] G. Gutierrez, B. Johansson, Phys. Rev. B 65 (2002) 104202.
[12] X. Zhao, D. Ceresoli, D. Vanderbilt, Phys. Rev. B 71 (2005) 085107.
[13] D. Vanderbilt, X. Zhao, D. Ceresoli, Thin Solid Films 486 (2005) 125.
[14] D. Ceresoli, D. Vanderbilt, Phys. Rev. B 74 (2006) 125108.
[15] V. Gritsenko, D. Gritsenko, S. Shaimeev, V. Aliev, K. Nasyrov, S. Erenburg, V. Tapilin, H. Wong, M.C. Poon, J.H. Lee, J.W. Lee, C.W. Kim, Microelectr. Eng. 81 (2005) 524.
[16] S.-M. Lee, D.G. Cahill, T.H. Allen, Phys. Rev. B 52 (1995) 253.
[17] Y. Oka, T. Takahashi, K. Okada, S. Iwai, J. Non-Cryst. Solids 30 (1979) 349.
[18] H. Momida, T. Hamada, Y. Takagi, T. Yamamoto, T. Uda, T. Ohno, Phys. Rev. B 73 (2006) 054108.
[19] S.P. Adiga, P. Zapol, L.A. Curtiss, Phys. Rev. B 74 (2006) 064204.
[20] G. Kresse, J. Furthmüller, Comput. Mat. Sci. 6 (1996) 15.
[21] G. Kresse, J. Furthmüller, Phys. Rev. B 54 (1996) 11169.
[22] Neugebauer, Scheffler, Phys. Rev. B 46 (1992) 16967.
[23] L.J. Alvarez, L.E. Leon, J.F. Sanz, M.J. Capitan, J.A. Odriozola, Phys. Rev. B 50 (1994) 2561.
[24] C. Ruberto, Y. Yourdshahyan, B.I. Lundqvist, Phys. Rev. B 67 (2003) 195412.
[25] H. Kim, C.O. Chui, K.C. Saraswat, P.C. McIntyre, Appl. Phys. Lett. 84 (13) (2003) 2647.
[26] Y. Kamata, Y. Kamimuta, T. Ino, A. Nishiyama, Jap. J. Appl. Phys. 44 (4B) (2005) 2323.
[27] Y. Kamata, Y. Kamimuta, T. Ino, R. Iijima, M. Koyama, A. Nishiyama, Jpn. J. Appl. Phys. 45 (7) (2006) 5651.
[28] J. Oh, P. Majhi, C.Y. Kang, J.-W. Yang, Appl. Phys. Lett. 90 (2007) 202102.
[29] J.J. Chen, N.A. Bojarczuk, H. Shang, M. Copel, J.B. Hannon, J. Karasinski, E. Preisler, S.K. Banerjee, S. Guha, IEEE Trans. Electr. Dev. 51 (9) (2004) 1441.